PERGAMON

International Journal of Heat and Mass Transfer 43 (2000) 1523–1535

International Journal of HEAT and MASS TRANSFER

www.elsevier.com/locate/ijhmt

Mixed convection in radial flow between horizontal plates — I. Numerical simulations

Helmar Van Santen, Chris R. Kleijn*, Harry E. A. Van Den Akker

Kramers Laboratorium voor Fysische Technologie, Delft University of Technology, Prins Bernhardlaan 6, 2628 BW Delft, Netherlands

Received 13 November 1998; received in revised form 16 July 1999

Abstract

A forced radially outward flow with secondary, buoyancy induced convection has been studied numerically in an axisymmetric geometry, consisting of two differentially heated, horizontal, coaxial, circular plates with a diameter of 25 times their mutual spacing. A forced laminar flow is supplied through the centre of the upper plate. The onset of thermal instability, leading to axisymmetric and three-dimensional rolls, has been determined as a function of the Reynolds, Prandtl and Rayleigh numbers. © 2000 Elsevier Science Ltd. All rights reserved.

1. Introduction

Buoyancy driven secondary convection in a forced laminar flow may lead to heat transfer enhancement and the onset of turbulence. The understanding of thermal and flow characteristics in this so-called mixed convection is of practical importance, e.g. in the design of compact heat exchangers and chemical vapor deposition reactors, or in the cooling of microelectronic equipment. In addition, these phenomena are of theoretical importance in view of assessing the different routes to turbulence. Accordingly, a number of theoretical, experimental and numerical studies have been carried out to investigate mixed convection [1–7].

In mixed convection, the nonlinear interaction of the laminar forced flow and free convection may cause a range of complex flow transitions. Examples are symmetry breaking in an otherwise symmetric geometry, the existence of multiple stable steady flows, and transition to transient or turbulent flows [8–10]. These types of instabilities highly depend on geometry and boundary conditions. Even with large aspect ratios, boundary conditions may determine the flow in the entire confinement. For example, at low Rayleigh numbers, the buoyancy induced flow between two large horizontal plates with isothermal vertical side-walls is completely different from that in the presence of insulated vertical side-walls [11]. Therefore, in practise, it is difficult to distinguish between the effect of the confinement and the interaction of the forced and the secondary flow.

In this paper, a numerical study is presented on the mixed convection flow in the geometry as schematically shown in Fig. 1. The geometry consists of two horizontal circular plates, the bottom plate being kept at a higher temperature than the top one. The diameter of the plates is large compared to their mutual distance. Through a hole in the middle of the top plate, a forced downward flow is supplied, which flows radially outward between the plates.

The forced flow is laminar and axisymmetric, and suppresses the onset of thermal instabilities. However, the characteristic velocity and with that the

* Corresponding author. Tel.: +31-15-278-2835; fax: +31-15-278-2838.

E-mail address: crkleijn@klft.tn.tudelft.nl (C.R. Kleijn).

0017-9310/00/$ - see front matter © 2000 Elsevier Science Ltd. All rights reserved.
PII: S0017-9310(99)00232-X

Nomenclature

a	Thermal diffusivity (m^2/s)	T	Temperature (K)
c	Constant	T_h	Temperature hot plate (K)
$\vec{e}_3$	Unitvector in the axial direction	T_c	Temperature cold plate (K)
g	Acceleration of gravity (m^2/s)	ΔT	Temperature difference (K)
H	Distance between the plates (m)	t	Dimensionless time
$N_{r,\theta,z}$	Number of grid cells in r-, θ-, z-direction	U	Characteristic velocity vector (m/s)
Pr	Prandtl number	$\vec{u}$	Dimensionless velocity vector
p	Dimensionless pressure	u_{in}	Dimensionless inlet velocity
Ra	Rayleigh number	v_r	Radial velocity (m/s)
Ra_{cr}	Critical Rayleigh number	z	Axial coordinate (m or –)
$Ra_{cr,trans}$	Critical Rayleigh number transversal rolls	α	Thermal expansion coefficient (1/K)
$Ra_{cr,long}$	Critical Rayleigh number longitudinal rolls	Φ_v	Volumetric flow rate (m^3/s)
		ν	Kinematic viscosity (m^2/s)
Re	Reynolds number	Θ	Dimensionless temperature
r	Radial coordinate (m or –)	θ	Circumferential coordinate (radians)
r_{max}	Maximum radial coordinate		

strength of the forced convection, decreases with the radial coordinate. The secondary flows, caused by buoyancy effects, are nonaxisymmetric and have a constant characteristic velocity throughout the geometry. The interaction of these two flows is determined as a function of the Reynolds, Grashof and Prandtl numbers.

In the study of mixed convection, the advantage of this geometry over the often used square duct is, that there are no vertical side walls to enforce a certain flow. This, however, is attained at the cost of some entrance effects. Applications of this geometry can be found, in (plasma enhanced) chemical vapor deposition reactors [12] and electro-chemical detectors [13]. As an example, CVD reactors are mostly axisymmetric and are often operated in the mixed convection flow regime. Detailed knowledge on flow transitions such as symmetry breaking therefore may be crucial for economical operation of these reactors.

2. Theoretical background

2.1. Flow between two differentially heated horizontal plates

In the absence of forced flow, the fluid between two infinite horizontal plates, the bottom plate being at a higher uniform temperature than the top one, becomes unstable when the buoyancy forces are sufficiently

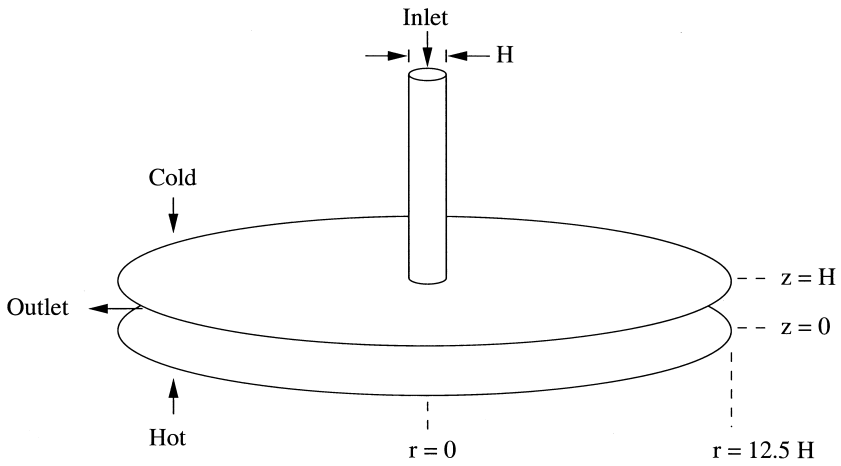

Fig. 1. Schematic of the geometry.

strong compared to the viscous forces. A linear stability analysis shows that the characteristic dimensionless group is the Rayleigh number ($Ra = gH^3\alpha\Delta T/\nu a$), and that its critical value, Ra_{cr}, is 1708 [14,15]. In an infinite geometry, this instability should lead to a directionally independent flow, e.g. corresponding to the well-known hexagonal Rayleigh–Bénard cells. At Rayleigh numbers slightly above critical, the flow pattern is steady. Increasing the Rayleigh number changes this pattern, and eventually, depending on the Prandtl number, the flow becomes transient.

In practise, there is always some effect of the boundaries, which may result in more irregular flow structures, or two-dimensional convection rolls [11,16]. For example, in a square duct with insulated side walls, irregular three-dimensional rolls are found, while cold or hot side walls enforce a particular direction of the buoyancy rolls. In general, the distance between the plates is the characteristic length of these flow structures.

In the presence of a forced flow, the transition is more complicated. In an infinite geometry, the critical Rayleigh number for disturbances perpendicular to the flow is still 1708, independent of the values of the Reynolds and Prandtl numbers. These disturbances lead to a steady 3D flow, with so-called longitudinal free convection rolls, i.e. rolls with their rotation axes in the direction of the flow [11]. The critical Rayleigh number for disturbances travelling along the direction of the flow, so-called transversal rolls, is higher, and is a function of the Reynolds and Prandtl numbers (see Fig. 2). The forced convection has a stabilising effect on disturbances travelling along the direction of the flow. In addition, increasing the Prandtl number stabilises these disturbances. In a good approximation to the data of Muralidhar and Kulacki [17], the critical Rayleigh number for transversal rolls, minus the critical Rayleigh number for longitudinal rolls, is proportional to the Prandtl number:

$$Ra_{cr,trans} - Ra_{cr,long} \approx Pr \times f(Re) \quad (1)$$

The flow pattern for Rayleigh numbers slightly above critical is steady, and consists of longitudinal rolls. Increasing the Rayleigh number eventually leads to transient flows, depending on the Reynolds and Prandtl numbers.

In a confined geometry, such as a square duct, the side walls are of influence. These may favour longitudinal, transversal, or irregular three-dimensional rolls. This changes Fig. 2, especially at low Reynolds numbers and at Rayleigh numbers near critical. Numerical and experimental examples can be found in Refs. [1,5,18].

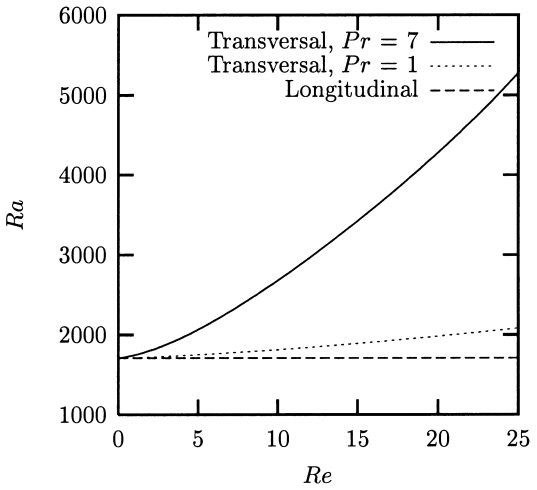

Fig. 2. Effect of *Re* and *Pr* on the critical Rayleigh number, after data from Muralidhar and Kulacki [17].

2.2. The geometry studied

In the absence of buoyancy induced flows, the forced flow in the geometry under study (see Fig. 1) is laminar and axisymmetric. The velocity field, after an entrance region and terms of order $1/r^3$ being ignored, corresponds to a Poiseuille profile, with the average velocity decreasing inversely proportional to radius r:

$$v_r(r,z) = \frac{1}{r}\frac{3\Phi_v}{\pi H^3} z(H-z) \quad (2)$$

with $v_r(r,z)$ the velocity in the r-direction, H the spacing of the two plates, and Φ_v the volumetric flow rate. The axisymmetry imposing effect of the forced flow decreases with r. This is not only due to the decreasing characteristic radial velocity, but also because the flow increasingly resembles the two-dimensional flow in a rectangular duct when the 'curvature ratio' H/r decreases.

In the absence of forced flow, the buoyancy induced flow resembles the standard Rayleigh–Bénard case. Small differences can be expected owing to the open boundary. In contrast to the forced flow, therefore, the buoyancy induced or secondary flow is not axisymmetric.

When both a forced flow and a temperature difference are applied, the forced and the free convection will interact. The resulting secondary flows may be separated in (i) transversal rolls, i.e. two-dimensional, axisymmetric torus-shaped rolls, and (ii) irregular, three-dimensional rolls. Longitudinal rolls, with axes of rotation in the direction of the radial forced flow, are unlikely, since the geometry would enforce an improbable wedge-like shape on these rolls. Longitudinal rolls therefore can be

expected to immediately transform into irregular three-dimensional rolls.

The critical Rayleigh number for the transversal, torus-shaped rolls may be related to the critical Rayleigh numbers for transversal rolls in Fig. 2. The Reynolds number, however, has to be corrected for the radial dependency of the characteristic forced flow velocity. This means that, for $Ra > Ra_{cr,long}$ and a fixed inflow rate, there is a radial coordinate where the characteristic velocity of the forced flow is sufficiently low to allow for transversal rolls. Save for differences owing to the circular shape of the rolls, Fig. 2 gives a good approximation for the Rayleigh and Prandtl dependency of this radial coordinate.

Once transversal rolls have been formed, they move radially outward, their radial velocity being related to the mean forced flow. The radial velocity of the rolls therefore can be expected to decrease with the radial coordinate, as the characteristic velocity of the forced flow decreases with the radial coordinate.

Provided that the flow remains axisymmetric, a conservation equation for the transversal rolls can be deduced. The number of rolls per unit of time that passes the first radial coordinate, equals the number of rolls per unit of time that passes the second radial coordinate minus the number of rolls that disappears per unit of time in between. For the flow to remain axisymmetric and the velocity of the rolls to decrease, therefore either the radial size of the rolls must decrease, or rolls must coalesce. The size of the rolls is not likely to decrease, since it is dictated by the spacing of plates. Therefore, when there are transversal rolls, symmetry breaking and/or roll coalescence is to be expected. This effect decreases with increasing radial coordinate.

There is a second mechanism that may lead to breakup of transversal rolls. Figure 2 shows that, in a parallel flow, the critical Rayleigh number for longitudinal rolls is unaffected by the flow. At larger radial coordinates, the forced flow resembles parallel flow. Therefore, even though purely longitudinal free convection rolls in this geometry are unlikely, at large radii, buoyancy induced flows can be expected, insensitive to the actual value of the Reynolds number. These secondary flows result in irregular, three-dimensional free convection rolls. In a square duct, the flow becomes transient and irregular when both transversal and longitudinal rolls may occur. Similarly, in the present geometry, transversal rolls can be expected to breakup when they pass the radial coordinate where three-dimensional rolls are possible. If the radial coordinate where these three-dimensional rolls may occur is smaller than the coordinate where transversal rolls are possible, transversal rolls even will be impossible at all.

3. Numerical method

3.1. Basic equations

The flow can be described by the Boussinesq approximated Navier–Stokes equations. Made dimensionless with characteristic distance H, a characteristic velocity U and the temperature difference $T_h - T_c$, these are as follows.

Conservation of mass

$$\nabla \cdot \vec{u} = 0 \tag{3}$$

Conservation of momentum

$$\frac{\partial \vec{u}}{\partial t} + \vec{u} \cdot \nabla \vec{u} = \frac{1}{Re} \nabla^2 \vec{u} - \nabla p + \frac{Ra}{Re^2 Pr} \Theta \vec{e}_3 \tag{4}$$

Conservation of energy

$$\frac{\partial \Theta}{\partial t} + \vec{u} \cdot \nabla \Theta = \frac{1}{Re \times Pr} \nabla^2 \Theta \tag{5}$$

The spacing of the plates is the obvious choice for the characteristic distance H. For the characteristic velocity U there are two possibilities, either that of the forced convection or that of the free convection. In this study, the characteristic velocity of the forced convection is selected. The magnitude of the buoyancy effects then can be isolated in Ra, whereas the magnitude of the forced flow is entailed in Re. Their relative importance is given by the so-called mixed convection parameter $Ra/(Re^2 Pr)$. In the geometry under investigation, the characteristic velocity for forced convection is a function of the radial position (see Eq. (2)). In order to characterise the flow uniquely, a single characteristic velocity has to be selected. In this paper, this is selected as $v_r(H,0.5H)$ in Eq. (2).

3.2. Discretisation

The geometry under investigation is axisymmetric, but the flow between the plates may not be axisymmetric. Therefore, the Navier–Stokes equations are solved in three-dimensional cylindrical coordinates. Disadvantage is the comparatively high number of cells required in the θ-direction. This, however, is compensated by the computational efficiency of orthogonal coordinates.

Equations (3)–(5) are discretised in space using a 2nd order accurate Finite Volume method on a staggered grid. For the time discretisation, the 2nd order accurate explicit leap-frog scheme with lagged diffusion terms is applied in the r- and z-direction [19]. To make the coupling between odd and even time-steps, an Asselin filter is used with a filter constant of 0.05 [20]. In the θ-direction, the 2nd order accurate implicit

Crank–Nicholson scheme is used to avoid strict time-step limitations.

The boundary conditions at the inlet, and at the lower and upper plate are Dirichlet boundary conditions:

$$z = 0 \rightarrow \Theta = 1; \vec{v} = \vec{0} \tag{6}$$

$$z = 1 \rightarrow \Theta = 0; \vec{v} = \begin{cases} u_{\text{in}}\vec{e}_3 & \text{if } r < \frac{1}{2}H \\ \vec{0} & \text{if } r \geq \frac{1}{2}H \end{cases}. \tag{7}$$

The outlet boundary requires careful treatment, as it is comparatively large, and structures have to be able to leave the domain undisturbedly, i.e. unaffected by the boundary condition [21]. Sani and Gresho [22,23] have shown that this can be attained by linear extrapolation of the outflow pressure, temperature and velocity. We have tested several outflow boundary conditions and have compared the results to simulations in a radially extended geometry. Our results confirmed, that linear extrapolation of outflow pressure, temperature and velocity performed best. Then, the effect of the outflow boundary condition only extended one to two times the platedistance back in the geometry.

The line $r = 0$ is singular in cylindrical coordinates. Therefore, the r-velocity required at this point is unavailable. This is solved by using an artificial r-velocity, obtained by linear interpolation across the centreline [24], i.e.

$$v_r(0,\theta_j,z_k) = \tfrac{1}{2}[v_r(\Delta r,\theta_j,z_k) - v_r(\Delta r,\theta_j + \pi,z_k)] \tag{8}$$

Fig. 3 shows instantaneous horizontal and vertical projections of the calculated velocities near $r = 0$, for a strongly three-dimensional flow field, illustrating that this approach leads to a smooth velocity field near the singular point.

3.3. Solution strategy

The resulting set of equations is solved with a predictor–corrector scheme. In the prediction step, the temperature for the new timestep and the intermediate r-, z- and θ-velocities are calculated. This corresponds to solving $N_r \times N_z$ tridiagonal systems for each of the four variables. In the correction step the new pressures are calculated by imposing mass conservation. These pressures correspond to a correction on the velocities to obey mass conservation exactly. In this step, a discrete Poisson equation has to be solved. This has been done with a Direct Fast Poisson solver, where the θ-transformation has been implemented as an FFT. The z-transformation is done with a matrix vector multiplication. This allows for a nonuniform grid in the z-direction, and is more efficient with the comparatively small amount of cells in this direction.

3.4. Parallelisation

The above method has been parallelised using domain decomposition in the r-direction. The resulting

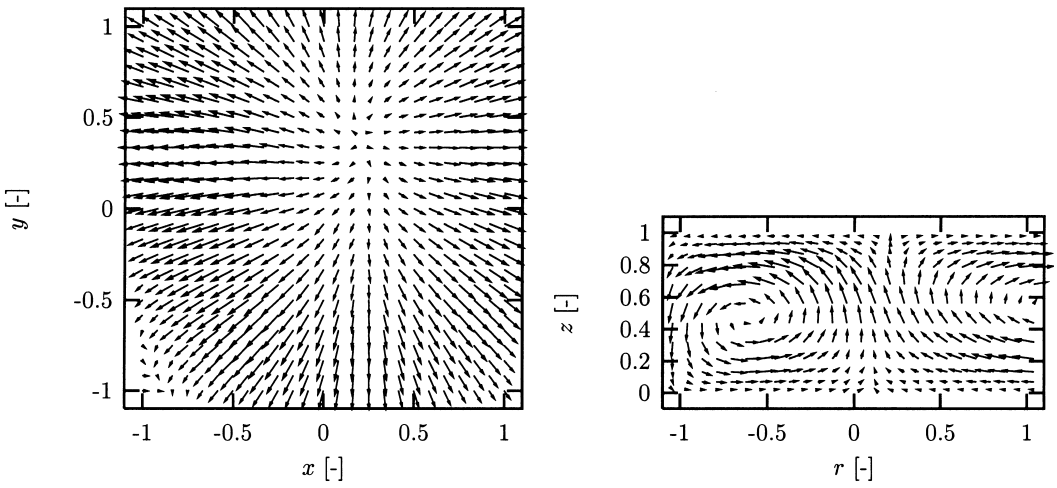

Fig. 3. Snapshot of the simulated flow field near the singular point $r = 0$ when there is no inflow. (a) Velocities in the r- and θ-direction, projected on an x–y grid at $z = 0.8$. (b) Velocities in the r- and z-direction.

ring-shaped grids are distributed over the different processors. In the prediction step, boundary data are exchanged between the processors, followed by solving the tridiagonal systems in each subdomain. In the correction step, a similar procedure is followed, apart from the r-transformation in the Fast Poisson Solver. In this step, information is required across the different subgrids. This is solved by decomposing the grid in the z-direction, just during this transformation. This requires one large send operation but on systems with a comparatively fast interprocessor connection this still leads to an efficient code.

The efficiency of the parallelisation has been tested on two parallel computers: an HP-Convex S-class server with four processors, and a Cray T3E. In Table 1, the speed-up is shown on a grid of $N_r \times N_z \times N_\theta = 100 \times 8 \times 400 = 3.2 \times 10^5$ points, which is the largest grid fitting in the memory of a single processor of the Cray. The table illustrates that a good speedup can be attained. The results presented below, mostly have been obtained on 8 processors of the Cray T3E.

3.5. Grid resolution

The grid used for the simulations contains $N_r \times N_z \times N_\theta = 150 \times 12 \times 600 = 1.08 \times 10^6$ points. The grid is nonuniform in the z-direction, in order to resolve the steep gradients near the walls. The following grid distribution function is used:

$$z_i = \frac{i-(1/2)}{N_z} - \frac{c}{2\pi}\sin\left(2\pi\frac{(i-(1/2))}{N_z}\right) \tag{9}$$

with $c = 1/2$.

This grid allows Reynolds numbers up to 100 and, as shown by Grötzback [25], Rayleigh numbers up to 25,000. At higher Reynolds numbers, the central scheme causes severe wiggles near the inlet, while at higher Rayleigh numbers the boundary layers are not sufficiently resolved [25]. Tests on a grid refined to $N_r \times N_z \times N_\theta = 250 \times 20 \times 1000$ resulted in a change in average Nusselt number below 3%, confirming that the selected grid is sufficiently fine. On the selected grid, a single time-step takes approximately 1.5 wall seconds on eight processors of the Cray T3E.

For the cases tested, of the order of 40,000 time steps are required to get a result which is independent of the start up conditions, taking about 20 h on eight processors of the Cray T3E. Hence, a limited number of cases could be studied only; these are given in Table 2.

Table 1
Parallelisation efficiency on two architectures

N_{proc}	Convex S-class		Cray T3E	
	Wall time (s)	Speed-up	Wall time (s)	Speed-up
1	2.84	1.0	2.65	1.0
2	1.54	1.8	1.46	1.8
4	0.95	3.0	0.78	3.4
8	–	–	0.44	6.0

Table 2
Parameter combinations studied

Case	*Re*	*Ra*	*Pr*
(1)	0	2500	0.7
(2)	40	3800	0.7
(3)	10	2000	0.7
(4)	50	2000	0.7
(5)	50	5000	0.7
(6)	100	2000	0.7
(7)	100	5000	0.7
(8)	10	2900	0.7
(9)	20	2900	0.7
(10)	35	2900	0.7
(11)	50	2900	0.7
(12)	60	2900	0.7
(13)	85	2900	0.7
(14)	100	2900	0.7
(15)	50	5000	2.0
(16)	50	17,500	7.0

4. Results

4.1. Rayleigh–Bénard case

In the absence of inflow, the flow in the present geometry should exhibit similar characteristics as the classical Rayleigh–Bénard case, i.e. the buoyancy driven flow between two infinite, differentially heated horizontal plates [14,15]. The difference is in the open circular boundary, which can be expected to cause deviations, as mixed convection flows are extremely sensitive to boundary conditions.

This has been tested at $Re = 0$, $Ra = 2500$ and $Pr = 0.7$ (case 1 in Table 2). The initial fields were selected axisymmetric: the variables in all points were set to zero. Time integration of the flow equations is continued until the final, quasiperiodic solution has become independent of the initial conditions.

As can be expected on account of the stress-free boundary conditions, the onset of instability is near the outlet of the reactor. This results in torus-shaped, approximately axisymmetric rolls. The flow field at this instant is illustrated in Fig. 4a, where the contours of

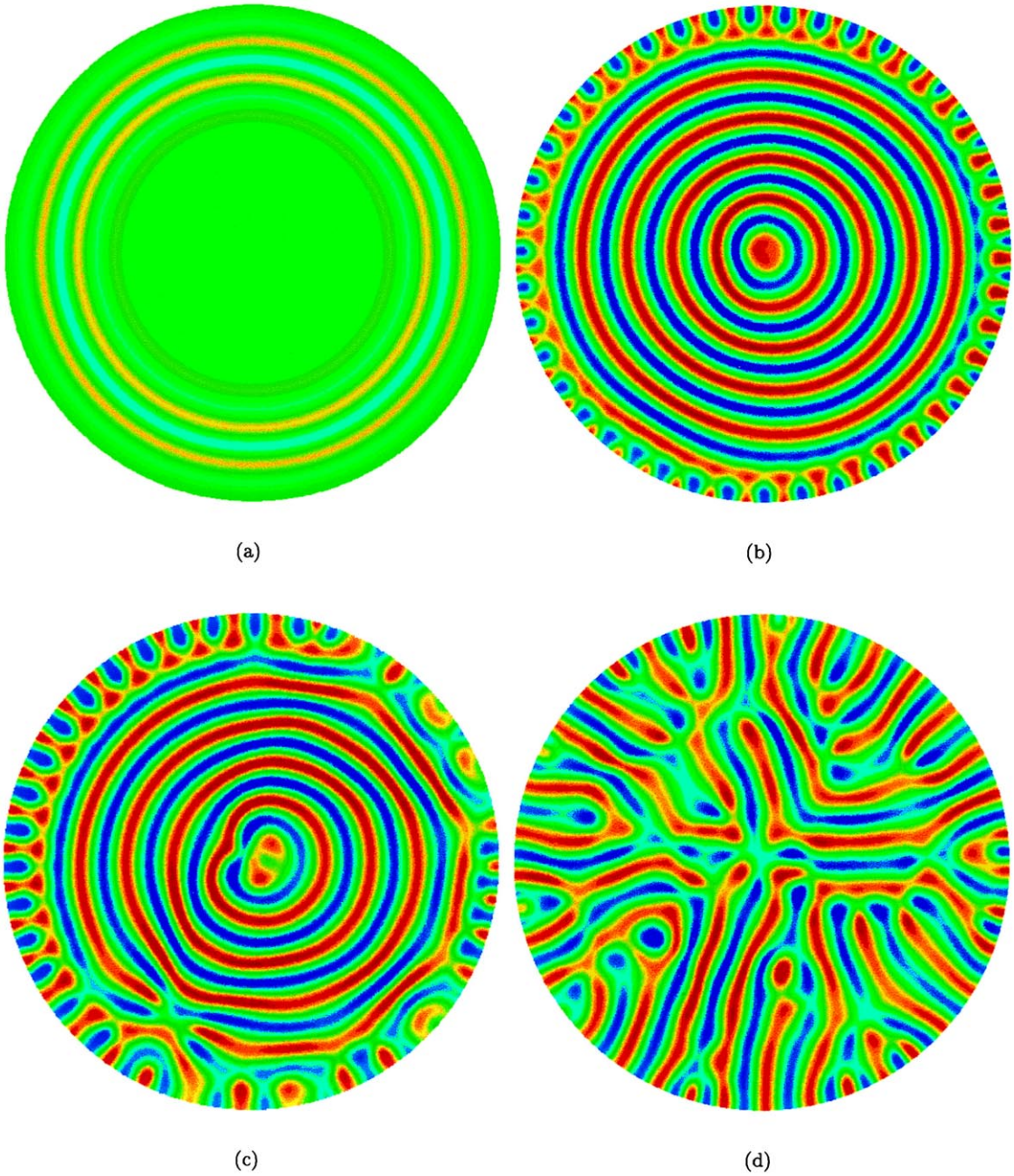

Fig. 4. Buoyancy induced flow in the absence of a forced flow at different stages of the onset of instability. $Pr = 0.7$ and $Ra = 2500$. Contour plot of the instantaneous z-velocities in a cross section at $z = 1/2$: $v_{min} = -0.12$; $v_{max} = 0.12$. (a) Initial, axisymmetric instability; (b) instability of the outer recirculation; (c) transition to nonaxisymmetric flow; (d) settled flow.

the z-velocities are plotted in a horizontal cross section at $z = 1/2$. The time, in the absence of forced flow made dimensionless with $[\sqrt{g\alpha\Delta T/H}]^{-1}$, needed for these instabilities to reach the centre is approximately 100. When the rolls have reached the centre, the large roll near the outlet becomes unstable and breaks up. The resulting flow is illustrated in Fig. 4b, again showing a contour plot of the z-velocities at $z = 1/2$.

The instability of the outer recirculation slowly moves inwards, while at the same time, the small

roll near $r = 0$ becomes unstable. This is illustrated in Fig. 4c. The dimensionless time to reach this state is about 300. Eventually, the flow turns completely non-axisymmetric and the recirculations are randomly ordered. This is shown in Fig. 4d, which is an instantaneous realisation of the transient flow field. For larger times, the characteristics of the flow remain essentially similar to those plotted in Fig. 4d.

The time scale needed for the initial conditions to damp out is large, typically a few hundred times the characteristic time scale of the recirculations. This is due to the long time needed for instabilities that start near the outlet to reach the centre. This has the advantage that, in the presence of a forced flow with $Re \gtrapprox 10$, the effect of the boundary on the flow is small.

As a result of the open boundary, the two-dimensional rolls or three-dimensional hexagons, typical of Rayleigh–Bénard convection, are not encountered. Fig. 4d shows that, in the absence of a mean flow, rolls have the tendency to direct their axis of rotation perpendicularly to the outlet area.

The average Nusselt number for the settled flow in Fig. 4d is 1.39 and remains approximately constant. This is in good agreement with the correlation as given by Hollands et al. [26], predicting a Nusselt number of 1.34. Compared to the initial conditions used in Fig. 4, the state with a settled Nusselt number can be reached within a fraction of the number of time steps by starting from a random initial field.

4.2. Thermal instability in the presence of a forced flow

4.2.1. General flow properties

The radially outward forced flow affects the position and shape of the secondary, buoyancy induced flows. This is illustrated in Fig. 5 for case 3: $Re = 10$, $Ra = 2000$, $Pr = 0.7$. The instantaneous contour plots of the z-velocities are plotted in a cross section at $z = 1/2$ after a time long enough for the initial transient to have damped out. The flow plotted in this figure may be separated into three areas with respect to the buoyancy induced flows. (i) For small radial coordinates, entrance effects and the forced flow suppress secondary flows (in Fig. 5 for $r \lessapprox 3$). In this area, the flow is steady and more or less axisymmetric. (ii) At intermediate radial coordinates, the secondary flow corresponds to more or less axisymmetric transversal rolls (in Fig. 5 for $3 \lessapprox r \lessapprox 8$). The transversal rolls move radially outward with the forced flow. (iii) At large radial coordinates, the secondary flow forms a three-dimensional chaotic pattern (in Fig. 5 for $r \gtrapprox 8$). The flow in this part remains transient and the forced flow, though low, still transports the flow structures radially outward. The effect of the Reynolds, Rayleigh and

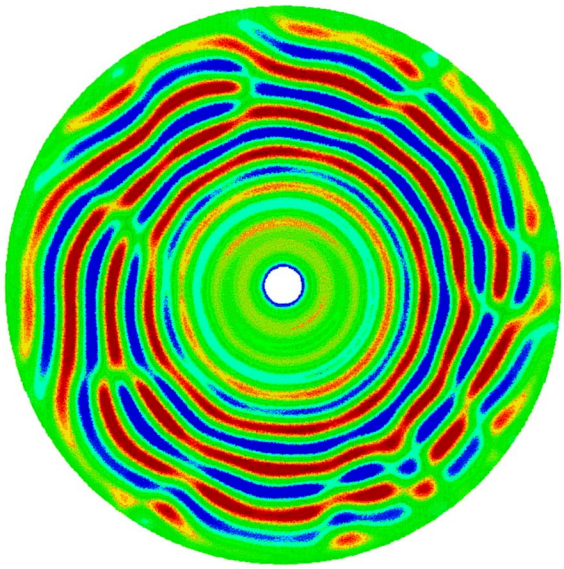

Fig. 5. Flow properties in the presence of a forced flow at $Re = 10$, $Pr = 0.7$, and $Ra = 2000$. Contour plot of the instantaneous z-velocities in a cross section at $z = 1/2$: $v_{min} = -0.07$: $v_{max} = 0.07$.

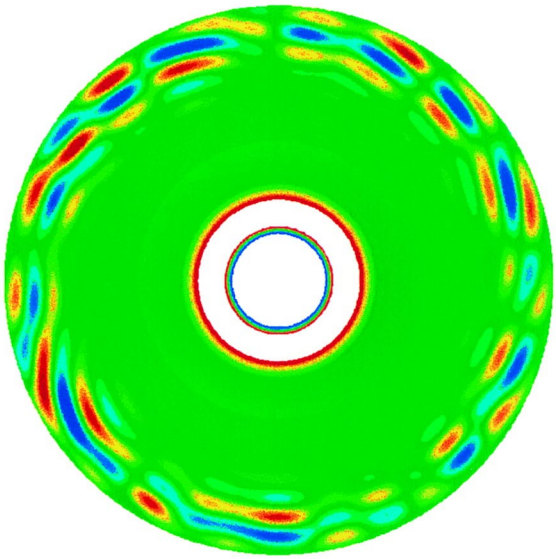

Fig. 6. Effect of the Reynolds number. $Re = 50$, $Pr = 0.7$ and $Ra = 2000$. Contour plot of the instantaneous z-velocities in a cross section at $z = 1/2$: $v_{min} = -0.03$; $v_{max} = 0.03$.

Prandtl numbers on the three areas in the flow is discussed below. Note that near the outlet, there is no tendency of recirculations to stand with their axis of rotation perpendicular to the outlet, as was found in the absence of a forced flow. This indicates that, even at this low Reynolds number, the effect of the open boundary on the flow within the geometry is small.

4.2.2. Effect of the Reynolds number

Increasing the Reynolds number can be expected to increase the effect of the forced flow. The part of the geometry that is dominated by entrance effects and the forced flow therefore will increase with Re. This is illustrated in Fig. 6 for case 4 where Ra and Pr are the same as in Fig. 5, while the Reynolds number is 50. As in Fig. 5, the instantaneous contour plots of the z velocities are plotted in a cross section at $z = 1/2$. The maximum and minimum velocities plotted, however, differ.

At this higher Reynolds number ($Re = 50$), the flow is stationary and axisymmetric in a large part of the reactor. At $r \approx 8$ the thermal instability of the forced flow becomes visible. The instability immediately leads to three-dimensional flow, skipping the area with axisymmetric rolls. The secondary flows, however, still show regularities, in the form of 'knots' at discrete angles with more or less equal intervals, and in the circular or spiral shape of the secondary flow. These regularities in the secondary flows are due to the symmetry imposing effect of the forced flow. However, the effect of the secondary flow on the forced flow at these conditions remains limited due to the low characteristic velocity of the buoyancy induced flow. This is illustrated in Fig. 7, where a contour plot is shown of the instantaneous r velocities in a cross section in the θ–z plane at $r = 0.8 \times r_{max}$.

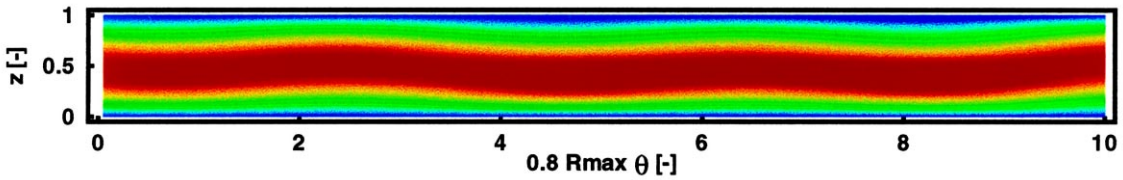

Fig. 7. Effect of secondary flows on the forced convection at $Re = 50$, $Pr = 0.7$ and $Ra = 2000$. Contour plot of the instantaneous r-velocities in a cross section in the θ–z plane at $r = 0.8 \times r_{max}$.

The results illustrated in Figs. 5 and 6 show that the Reynolds number affects the occurrence of transversal rolls. Transversal rolls can be found, if the Reynolds number is sufficiently low to allow for transversal rolls for small radial coordinates or high curvature numbers. Otherwise, the secondary flows will be three-dimensional. The cases tested indicate that for $Pr = 0.7$, transversal rolls occur only when the Reynolds number is sufficiently low for them to be formed at $r/H \lessapprox 1/5$.

4.2.3. Effect of the Prandtl number

In a parallel flow, the critical Rayleigh number for longitudinal rolls is independent of the Prandtl number, while the critical Rayleigh number for transversal rolls is approximately proportional to Prandtl (see Eq. (1)). The effect of increasing Prandtl in the present geometry is illustrated in Fig. 8 for cases 15 and 16. Reynolds is 50, while Rayleigh is scaled in order to keep Ra/Pr constant. For $Pr = 2$ (Fig. 8a) and $Pr = 7$ (Fig. 8b), the instantaneous contour plots of the z-velocities are plotted in a cross section at $z = 1/2$.

At $Pr = 2$, the thermal instability of the forced flow results in torus-shaped recirculations (see Fig. 8a). At a larger radial distance, these torus-shaped rolls break up and form a more chaotic pattern. This is similar to the case $Re = 10$, $Pr = 0.7$ and $Ra = 2000$ (see Fig. 5), though the torus-shaped rolls at this higher Prandtl number are more axisymmetric and stable.

Fig. 8a is an instantaneous realisation of the transient flow field. Time series also show the breakup of the axisymmetric transversal rolls. This is illustrated in Fig. 9, where temperature has been plotted as a function of the dimensionless time at position $z = 1/2$, $\theta = \pm(\pi/2)$, and $r = 0.6$ and $0.8 \times r_{max}$, respectively. The time is made dimensionless with the plate separation H and $v_r(H,0.5H)$ in Eq. (2).

The simulation is started from a settled flow at $Re = 50$, $Pr = 0.7$, and $Ra = 2000$. Figure 9 shows that it takes 50 dimensionless time units for the initial conditions to damp out. Once the flow has settled, the transversal rolls at $r = 0.6 \times r_{max}$ are torus-shaped and almost symmetric and pass the locations at $\theta = (\pi/2)$ and $\theta = -(\pi/2)$ with the same frequency, though with small phase differences (see also Fig. 8a). At position $r = 0.8 \times r_{max}$, the flow is completely three-dimensional and there is little correlation between the signals at $\theta = \pi/2$ and $\theta = -(\pi/2)$.

From the frequency at $r = 0.6 \times r_{max}$, it can be derived that the velocity of the rolls is 0.9 times the aver-

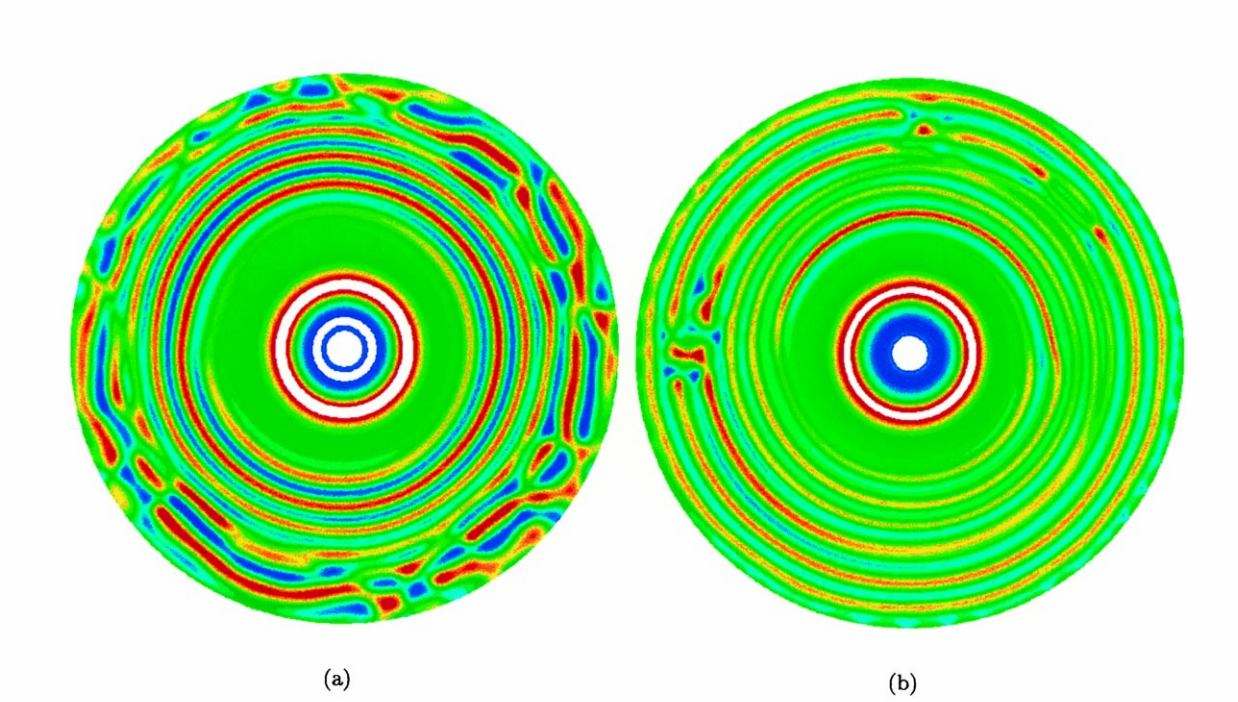

Fig. 8. Effect of the Prandtl number. $Re = 50$. Contour plot of the instantaneous z-velocities in a cross section at $z = 1/2$. (a) $Pr = 2$, $Ra = 5000$, $v_{min} = -0.12$; $v_{max} = 0.12$. (b) $Pr = 7$, $Ra = 17{,}500$, $v_{min} = -0.12$; $v_{max} = 0.12$.

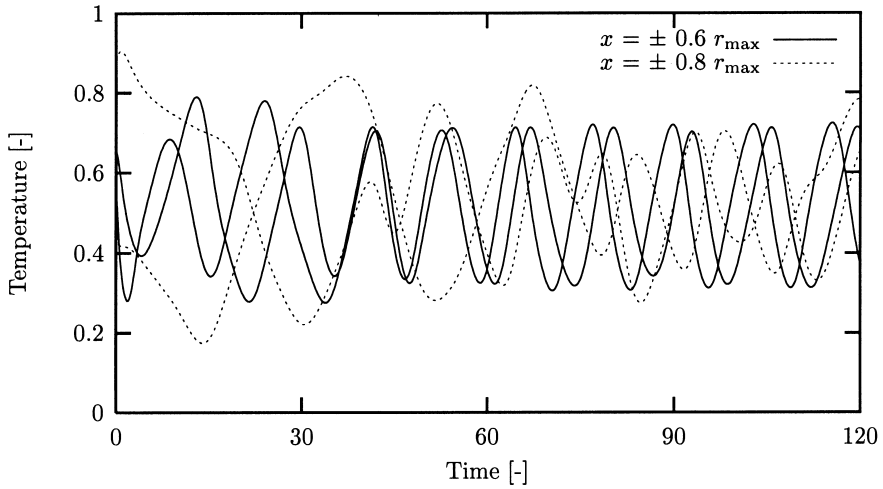

Fig. 9. Time series of the temperature at position $z = 1/2$, and $x = 0.6$, -0.6, 0.8 and $-0.8 \times r_{max}$. $Re = 50$, $Pr = 2$ and $Ra = 5000$.

age radial velocity at that position. Also in the experiments by Luijkx et al. [1], the velocity of transversal rolls was found to be of the order of the average fluid velocity. The exact frequency, however, is a function of the three operating parameters.

Increasing the Prandtl number further to 7 leads to transversal rolls that, apart from a few disturbances, remain intact throughout the geometry (see Fig. 8b). The disturbances that lead to isolated 'asymmetry spots' probably can be attributed to the fact that the forced velocity and thus the velocity of the rolls have to decrease as a function of the radial coordinate. As was argued in Section 2.2, for the velocity of the transversal rolls to decrease and for the flow to remain symmetric, rolls have to disappear. This indeed happens as illustrated in Fig. 10 where the velocities in the r- and z-direction are shown in a cross section. Several rolls are pushed away by the main flow between $r = 7$ and $r = 10$. At these operating conditions, this leads to a few small instabilities.

An explanation for the observed Prandtl dependency may be related to the role of the Prandtl number in the energy equation (see Eq. (5)). Compare the flow with a high and a low Prandtl number with identical Grashof and Reynolds numbers. The magnitude of the buoyancy term in the momentum equation is the same for both cases. In the energy equation, however, a high Prandtl number enlarges the effect of the convection terms relative to the diffusion terms. When the forced flow is important and when the initial instability is symmetric, the convection terms may enhance axisymmetry.

4.2.4. Effect of the Rayleigh number

Increasing the Rayleigh number corresponds to increasing the importance of the free convection compared to the forced convection. The radial coordinate where transversal rolls may occur may decrease (see Fig. 2). In addition, the radial coordinate where the asymmetric flow corresponding to just free convection rolls can be expected to decrease as well.

This is illustrated for case 5 in Fig. 11. A contour plot is plotted of the instantaneous z-velocities at $z = 1/2$. Fig. 11 has $Pr = 0.7$, $Re = 50$ and $Ra = 5000$. Compared to case 4 in Fig. 6b, at $Ra = 2000$, the onset of thermal instability is more torus-shaped. This is the result of the entrance effects. The torus-shaped rolls, however, quickly become unstable. At larger

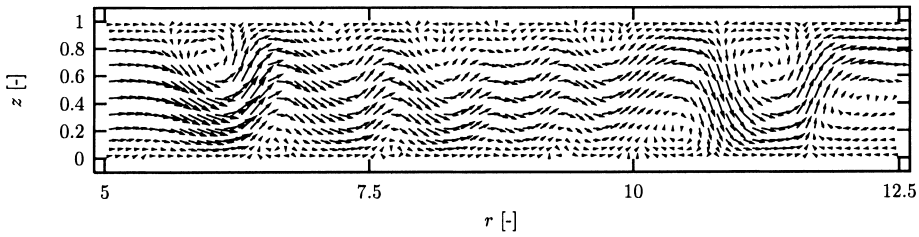

Fig. 10. Forced flow, pushing away buoyancy induced transversal rolls. $Re = 50$, $Pr = 7$ and $Ra = 17{,}500$.

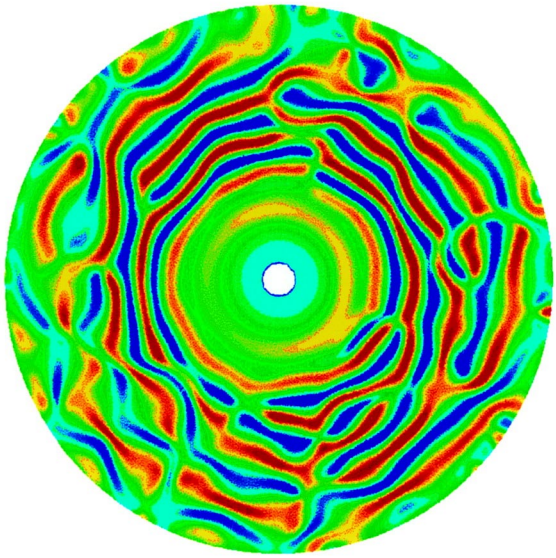

Fig. 11. Effect of the Rayleigh number. $Re = 50$, $Pr = 0.7$, $Ra = 5000$. $v_{min} = 0.12$; $v_{max} = 0.12$. Contour plot of the instantaneous z-velocities in a cross section at $z = 1/2$.

radial coordinates, the chaotic flow of plain Rayleigh–Bénard convection at $Ra = 5000$ prevails.

5. Concluding remarks

Detailed numerical simulations yielded insight to the interaction of forced radially outward flow with secondary, buoyancy induced convection. The axisymmetric forced flow affects the secondary, three-dimensional buoyancy induced convection. Close to the inlet, buoyancy effects are suppressed, whereas for small radial coordinates the buoyancy induced secondary flows are regulated into almost axisymmetric torus-shaped rolls. Only at larger radial coordinates the more irregular pattern corresponding to just buoyancy induced convection takes over. This is not only a result of the decreasing characteristic velocity of the forced flow, but also of the decreasing curvature of the mean forced flow, relative to the spacing of the plates.

The axisymmetry imposing effect of the forced flow increases with increasing Prandtl number, resulting at $Pr = 7$ even to an almost fully axisymmetric flow. This probably can be attributed to the role of the Prandtl number in the energy equation where Prandtl increases the effect of the axisymmetric advective terms. The axisymmetry decreases with increasing Rayleigh number as the Rayleigh number increases the importance of the nonaxisymmetric free convection.

Acknowledgements

The authors wish to thank the centre for High Performance Applied Computing (HPαC) of Delft University of Technology for being able to use their computing facilities.

References

[1] J.M. Luijkx, J.K. Platten, L.Cl. Legros, On the existence of thermoconvective rolls, transverse to a superimposed mean poiseulle flow, Int. J. Heat Mass Transfer 24 (1981) 1287–1291.
[2] K.C. Chiu, F. Rosenberger, Mixed convection between horizontal plates, I: entrance effects, Int. J. Heat Mass Transfer 30 (1987) 1645–1654.
[3] K.C. Chiu, J. Ouazzani, F. Rosenberger, Mixed convection between horizontal plates—II. Fully developed flow, Int. J. Heat Mass Transfer 30 (1987) 1655–1662.
[4] M.T. Ouazzani, M.T. Caltagirone, G. Meyer, A. Mojtabi, Etude numérique et expérimentale de la convection mixte entre deux plans horizontaux à températures différentes, Int. J. Heat Mass Transfer 32 (1989) 261–269.

[5] G.H. Evans, R. Greif, A study of traveling wave instabilities in a horizontal channel flow with applications to chemical vapor deposition, Int. J. Heat Mass Transfer 32 (5) (1989) 895–911.
[6] M.T. Ouazzani, J.K. Platten, A. Mojtabi, Etude expérimentale de la convection mixte entre deux plans horizontaux à températures différentes—II, Int. J. Heat Mass Transfer 33 (1990) 1417–1427.
[7] M.T. Ouazzani, J.K. Platten, H.W. Müller, M. Lücke, Etude de la convection mixte entre deux plans horizontaux à températures différentes, III, Int. J. Heat Mass Transfer 38 (1995) 875–886.
[8] D.I. Fotiadis, A.M. Kremer, D.R. McKenna, K.F. Jensen, Complex flow phenomena in vertical MOCVD reactors: effects on deposition uniformity and interface abruptness, J. Crystal Growth 85 (1987) 154–164.
[9] H. Van Santen, C.R. Kleijn, H.E.A. Van Den Akker, Mixed convection flow instabilities in chemical vapor deposition reactors, in: Book of Late News Abstracts 10th European Conference on CVD, Venice, Italy, 1995, p. 58.
[10] Y. Yamaguchi, C.J. Chang, R.A. Brown, Multiple buoyancy-driven flows in a vertical cylinder heated from below, Phil. Trans. R. Soc. Lond. A 312 (1984) 519–552.
[11] J.M. Luijkx, J.K. Platten, On the onset of free convection in a rectangular channel, J. Non-Equilib. Thermodyn. 6 (1981) 141–158.
[12] J.L. Vossen, W. Kern, Thin Film Processes, Academic Press, New York, 1978.
[13] A.J. Dalhuijsen, Th.H. Van Der Meer, C.J. Hoogendoorn, J.C. Hoogvliet, W.P. Van Bennekom, Hydrodynamic properties and mass transfer characteristics of electrochemical flow through cells of the confined wall-jet type, J. Electroanal. Chem. 182 (1985) 295–313.
[14] S. Chandrasekhar, Hydrodynamic and Hydromagnetic Stability, Clarendon Press, Oxford, 1961.
[15] P.G. Drazin, W.H. Reid, Hydrodynamic Stability, Cambridge University Press, Cambridge, 1981.
[16] J.K. Platten, J.C. Legros, Convection in Liquids, Springer-Verlag, Berlin, 1984.
[17] K. Muralidhar, F.A. Kulacki, Stability of mixed convection flow, Heat and Fluid Flow 8 (1987) 228–234.
[18] J.M. Luijkx, J.K. Platten, L.Cl. Legros, Precise measurements of the wavelength at the onset of Rayleigh–Bénard convection in a long rectangular duct, Int. J. Heat Mass Transfer 25 (1982) 1252–1254.
[19] C. Hirsch, Numerical Computation of Internal and External Flows, vol. 1, Fundamentals of Numerical Discretization, Wiley, Chichester, 1988.
[20] R. Asselin, Frequency filter for time integrations, Mon. Weather Rev. 100 (1972) 487–490.
[21] G.H. Evans, S. Paolucci, The thermoconvective instability of plane Poiseuille flow heated from below: a benchmark solution for open boundary flows, Int. J. Num. Meth. Fluids 11 (1990) 969–980.
[22] R.L. Sani, P.M. Gresho, Résumé and remarks on the open boundary condition minisymposium, Int. J. Num. Meth. Fluids 18 (1994) 983–1008.
[23] P.M. Gresho, R.L. Sani, On pressure boundary conditions for the incompressible Navier–Stokes equations, Int. J. Num. Meth. Fluids 7 (1987) 1111–1145.
[24] J. G. M. Eggels. Direct and large eddy simulation of turbulent flow in a cylindrical pipe geometry. Ph.D. thesis, Delft University of Technology, 1994.
[25] G. Grötzback, Spatial resolution requirements for direct numerical simulation of the Rayleigh–Bénard convection, J. Comp. Phys. 49 (1983) 241–264.
[26] K.G.T. Hollands, G.D. Raithby, L. Konicek, Correlation equation for free convection heat transfer in horizontal layers of air and water, Int. J. Heat Mass Transfer 18 (1976) 879–884.